ORIGINAL RESEARCH ARTICLE

Fabrication of CoO$_x$/BiVO$_4$ Photoanodes with Enhanced Photoelectrochemical Water Splitting

Meirong Sui[1] · **Xiuquan Gu**[2]

Abstract

In this work, the surface of BiVO$_4$ nanoporous films was modified by ultrathin CoO$_x$ nanoparticles through a facile electrochemical deposition route. By adjusting the deposition time, the effect of CoO$_x$ loading amount (or time) was investigated with respect to the photoelectrochemical (PEC) performance of the BiVO$_4$ photoanode. No significant morphological changes were observed after depositing CoO$_x$ cocatalysts onto the BiVO$_4$ surface, except for a rougher surface and the appearance of nanosheets at 40 s. After optimizing the deposition time, the highest photocurrent density of 3.36 mA/cm^2 was achieved at 1.23 V_{RHE} for the 20-CB sample under solar irradiation, exhibiting a nearly threefold increase in the photocurrent as compared to that of pristine BiVO$_4$ (1.24 mA/cm^2). It was found that the CoO$_x$ loading reduced the onset potential and interfacial charge transfer resistance, leading to the significant enhancement of the PEC activity. However, when the deposition time was extended or the loading amount increased, the PEC activity actually decreased, which might be related to the increase in carrier recombination loss. This research will help us understand the mechanism of surface CoO$_x$ modification for improving the PEC activity of semiconductor photoanodes like BiVO$_4$.

Keywords BiVO$_4$ · CoO$_x$ · photoelectrochemical · heterostructure · cocatalyst

Introduction

Currently, the increasing energy shortage has caused people to turn their attention towards clean energy like solar and hydrogen energies. Photoelectrochemical (PEC) water splitting provides a feasible method for utilizing solar energy to produce H$_2$, which is usually carried out in a two-electrode or three-electrode system.[1,2] The H$_2$ production rate is usually faster than powder-based photocatalytic systems and cheaper than electrocatalysis.[3] At present, PEC water splitting is faced with challenges in developing a suitable photoelectrode candidate that has broad light-harvesting ability, suitable bandgap, and high catalytic activity, and which can quickly split water into H$_2$ or O$_2$ under illumination. Currently, the solar-to-hydrogen (STH) efficiency of

PEC cells is still limited by the photoanode, which involves a four-electron transfer process rather than a two-electron transfer process that occurs on the cathode.[4] As is commonly known, it is difficult to achieve ideal PEC activity in photoanodes with a single component like ZnO, TiO$_2$, or BiVO$_4$, because they have certain limitations, including narrow spectral response, slow carrier separation, and possible photo-corrosion behavior. In most cases, surface engineering techniques such as metal deposition, doping, and the construction of a heterojunction or nanocomposites are commonly employed for enhancing both the PEC activity and stability of a semiconductor electrode.[5–7]

BiVO$_4$ is a hot candidate for fabricating solar water-splitting photoanodes due to its suitable bandgap of 2.4 eV, good stability, environmentally friendly nature, and low cost. In theory, the conversion efficiency of the BiVO$_4$ photoanode from sunlight can reach 9.2%, corresponding to a photocurrent of 7.5 mA/cm^2 under solar irradiation.[8] However, the PEC performance of BiVO$_4$ is limited by the slow water oxidation kinetic on its surface, which could be enhanced significantly by modifying its surface with cocatalysts.[9] To date, much effort has been devoted to optimizing BiVO$_4$ photoanodes and exploring the underlying mechanism.

✉ Meirong Sui
smr2012@xzhmu.edu.cn

1 School of Medical Imaging, Xuzhou Medical University, Xuzhou 221004, China

2 School of Materials Science and Physics, China University of Mining and Technology, Xuzhou 221116, Jiangsu Province, China

He et al. developed a novel, high-efficiency, solar-driven BiVO$_4$-related photoanode via sandwiching a photothermal CoO$_x$ layer between a BiVO$_4$ photoanode film and an FeOOH/NiOOH sheet electrocatalyst, leading to a superior photocurrent density of 6.34 mA/cm^2 at 1.23 V versus a reversible reference electrode (V_{RHE}).[10] In their study, CoO$_x$ plays at least two roles in enhancing the PEC activity of BiVO$_4$ photoanodes. First, CoO$_x$ can be used as a photothermal material, utilizing the heat in the solar spectrum, which corresponds to the energy over the infrared band. Second, CoO$_x$ also has a strong hole-extraction capability, making it a suitable hole cocatalyst with suitable valence band edges (VBE). In another report, Song et al. demonstrated a high photocurrent density of 5.85 mA/cm^2 at 1.23 V_{RHE} under solar irradiation in a BiVO$_4$ nanoporous photoanode through incorporating MoO$_x$/MXene quantum dots (MQD) into the hole transfer layer.[11] In addition, Seo et al. found that the colloidal CeO$_2$ quantum dot (CeQD) layer simultaneously enhanced the charge-separation efficiency and transfer kinetics, resulting in the highest photocurrent density (4.0 mA/cm^2) at 1.23 V_{RHE} under visible light irradiation.[12] In their study, the CeQDs with average sizes of 1.8–3.0 nm served as the hole extraction layer. However, there are currently few reports on surface modification of BiVO$_4$ photoanodes with CoO$_x$ or Co$_3$O$_4$ cocatalysts, and the mechanism requires a deeper investigation. More attention has been directed towards other surface modifiers (cocatalysts) like CoO$_x$, Co$_3$O$_4$, CoPi, and CoOOH.[13–15]

In this work, BiVO$_4$ nanoporous films were modified with thin CoO$_x$ nanoparticles (NPs) via a facile electrochemical deposition route. The existence of CoO$_x$ was firstly demonstrated by x-ray diffraction (XRD) patterns. After loading of a suitable amount of CoO$_x$ cocatalyst, the CoO$_x$-modified BiVO$_4$ photoanode displayed the highest photocurrent density of ~3.36 mA/cm^2 at 1.23 V_{RHE} under simulated solar irradiation. The enhanced PEC performance was attributed to the reduced interface charge transfer resistance, as indicated by the electrochemical impedance spectroscopy (EIS) results.

Experimental Details

Preparation of BiVO$_4$ Nanoporous Photoanodes

The nanoporous BiVO$_4$ photoanodes used in this work were prepared according to our previous work.[16] Briefly, the BiOI intermediate was obtained through electrodeposition and then converted into a BiVO$_4$ porous film by a solution drop-casting process. Specifically, a 0.04 mol/L Bi(NO$_3$)$_3$ solution was prepared by slowly dissolving Bi(NO$_3$)$_3$·5H$_2$O in 50 mL of 0.4 mol/L KI aqueous solution with pH of 1.75. Then, 20 mL of absolute ethanol containing 0.23 mol/L p-benzoquinone was mixed into the solution. The BiOI electrodeposition onto a fluorine-doped tin oxide (FTO) glass substrate was carried out in a three-electrode electrochemical cell consisting of a working electrode (WE), counter electrode (CE), and reference electrode (RE) at −0.143 V versus a saturated calomel electrode (SCE) for 10 min. Then, 0.15 mL of VO(acac)$_2$/DMSO solution (0.2 mol/L) was dripped onto the BiOI films (2 × 2 cm^2), followed by drying in an oven (60°C, 3 h) and annealing in air (450°C, 2 h). Finally, the pristine BiVO$_4$ electrodes were obtained by soaking the samples into a 1.0 mol/L NaOH aqueous solution for 30 min in order to remove the excess of V$_2$O$_5$.

Deposition of CoO$_x$ on BiVO$_4$ Photoanode

The deposition of the CoOx nanosheet on the BiVO$_4$ photoanode comprised two steps.[11] First, the Co(OH)$_2$ nanosheet was produced by electrochemical deposition. The as-prepared BiVO$_4$ photoanode was used as the working electrode, the SCE as a reference electrode, and Pt foils as counter electrode. The electrolyte solution was prepared by dissolving Co(NO$_3$)$_2$·6H$_2$O (15 mM) in deionized (DI) water. The working electrode was applied at a constant voltage (−1.0 V versus SCE) and the amount of Co(OH)$_2$ deposited was controlled by varying the deposition time from 5 s to 40 s. Second, the obtained Co(OH)$_2$/BiVO$_4$ film was rinsed with DI water and dried in air, followed by an annealing process in a muffle furnace at 350°C with a ramping rate of 2°C/min for 2 h. Finally, the CoO$_x$/BiVO$_4$ photoanode samples were designated as BVO, 5-CB, 10-CB, 20-CB, 30-CB, and 40-CB, respectively, according to the CoO$_x$ deposition time.

Material Characterization

The structural analysis of samples was carried out by X-ray diffraction (XRD, Haoyuan DX-2700) with a Cu Kα source. The surface morphology of the as-prepared photoanodes was determined by field-emission scanning electron microscopy (FESEM, Hitachi SU8220 next-generation, Japan) equipped with X-ray energy-dispersive spectroscopy (EDS) system. The light absorption properties of as-prepared samples were measured by ultraviolet–visible (UV–Vis) diffuse reflectance spectroscopy (DRS, Cary 300 UV–Vis spectrophotometer, Varian Co.), in which a BaSO$_4$ whiteboard was used as the internal reflectance standard.

PEC Measurements

The PEC measurements of photoanodes were performed using a CHI 660E electrochemical workstation in a standard three-electrode system. The obtained photoanode working electrode, SCE reference electrode, and a Pt foil counter electrode were used. An aqueous solution of 0.1 M Na_2SO_4 (pH = 7) was used as the electrolyte after N_2 bubbling for 0.5 h. The intensity of simulated sunlight was controlled at 100 mW/cm^2 using a 300 W Xe arc lamp with an AM 1.5G filter (CHF-XM-500 W, Beijing Changtuo Technology Co., Ltd.). All photoanodes were illuminated by simulated sunlight through the FTO side (i.e., a backside illumination). The tested area of the photoanode controlled by epoxy resin was about 6.0 cm^2. The photocurrent–potential curves were measured by scanning with a continuous voltage change at a scan rate of 20 mV/s. The measured potentials versus SCE electrode were converted to the reversible hydrogen electrode (RHE) using the Nernst equation:

$$V_{RHE} = V_{NHE} + 0.059\, pH = V_{SCE} + 0.059\, pH + 0.24 \quad (1)$$

where V_{RHE} is the converted potential versus RHE, and V_{SCE} is the experimentally measured potential against the SCE reference electrode. In addition, the electrochemical impedance spectra were recorded under irradiation over a frequency range of 0.1–5 × 10^4 Hz with an amplitude of 20 mV and an applied potential of 0.0 V versus SCE.

Results and Discussion

Structure and Surface Morphology

The $BiVO_4$ photoanode was prepared via the electrodeposition solution drop-casting process. Figure 1 presents the FESEM images of $BiVO_4$ and CoO_x/$BiVO_4$ heterostructure photoanodes. Pure $BiVO_4$ possesses a network structure composed of interconnected rod-like particles (200–300 nm in diameter) with a smooth surface and no impurities present on its surface. The nanoporous structure and vertically oriented worm-like morphology of the $BiVO_4$ photoanode was retained even after loading of a large amount of CoO_x cocatalysts. Such a surface morphology is beneficial for obtaining a large surface area and electrolyte infiltration. The above results also indicate that the CoO_x cocatalyst is so small that it does not block the pores of $BiVO_4$ and could not be distinguished by SEM. It was also found that the CoO_x loading would roughen the $BiVO_4$ particle surface, but there were no CoO_x nanosheets until the electrodeposition time reached 40 s (Fig. 1f).

Figure 2 compares the XRD patterns of $BiVO_4$ and the $BiVO_4$/CoO_x heterostructure with different deposition times (from 5 s to 40 s). For the pure $BiVO_4$ sample, all the diffraction peaks are assigned to the monoclinic scheelite crystal structure (JCPDS no. 14-0688) of $BiVO_4$ and the rutile crystal structure (JCPDS no. 41-1445) of SnO_2 derived from the FTO. No diffraction peaks of other phases or impurities were observed, indicating the high crystal quality and purity of the samples. There are no obvious peaks of CoO_x species in the XRD pattern, which might be ascribed to a low deposition amount of $Co(OH)_2$ as well as overlapping
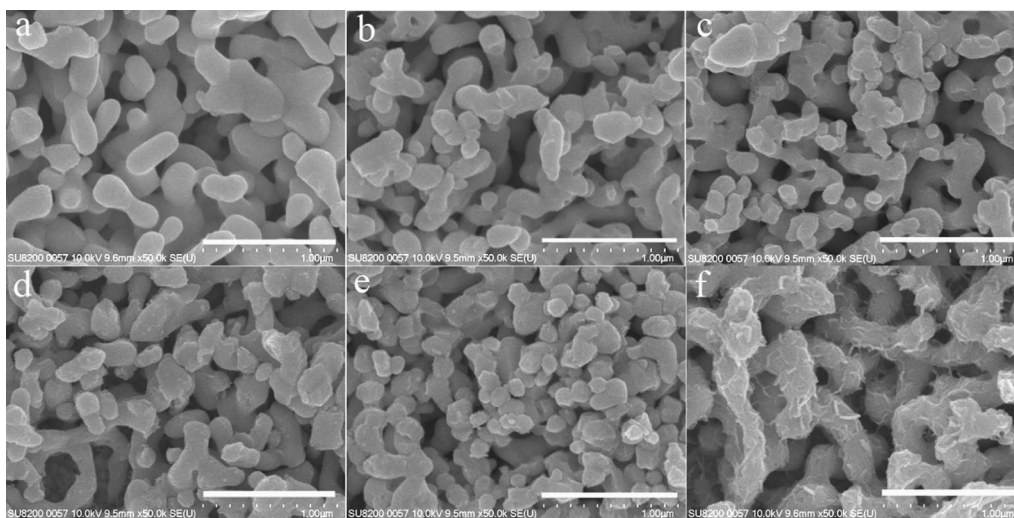

Fig. 1 Typical FESEM images of (a) $BiVO_4$ and (b–f) $BiVO_4$ modified with different deposition time of CoO_x: (b) 5 s, (c) 10 s, (d) 20 s, (e) 30 s, and (f) 40 s. The scale is 1 μm.
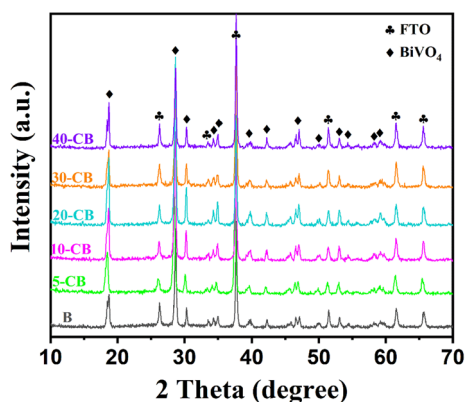
Fig. 2 XRD patterns of BiVO$_4$ porous photoanodes with and without CoO$_x$ modification. The character "40-CB" represents the sample with an electrodeposition time of 40 s.
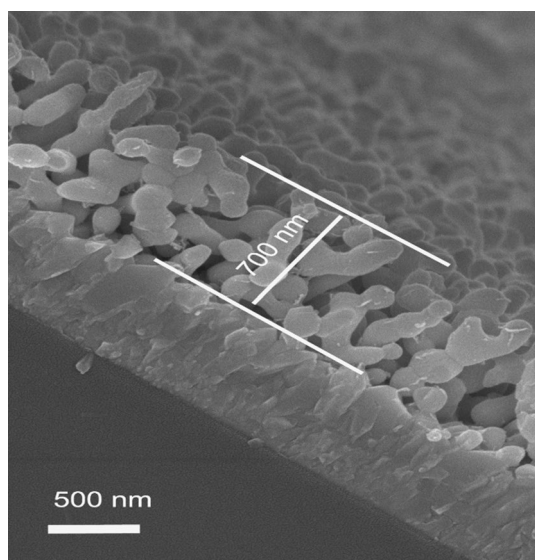

Fig. 3 Cross-sectional SEM image of a BiVO$_4$ photoanode modified with CoO$_x$ cocatalyst (40-CB).

of the CoO$_x$-related peaks with those of BiVO$_4$. It is worth noting that the dominant peak of CoO$_x$ located at 18.9° was overlapped with the (011) crystal plane of BiVO$_4$.

Figure 3 displays the cross-sectional SEM image of a typical CoO$_x$/BiVO$_4$ sample (40-CB). As can be seen, the BiVO$_4$ film, the FTO conductive layer, and glass substrate are identified with clear interfaces. The BiVO$_4$ nanoporous film displays a thickness of ~700 nm and worm-like porous morphology, where a small amount of CoO$_x$ nanosheets appear on the BiVO$_4$ microparticles.

Figure 4 presents the surface morphology of a typical BiVO$_4$/CoO$_x$ sample (40-CB) and its EDS elemental mapping results. As shown in Fig. 4a, the CoO$_x$ nanosheets are identified on the surface of BiVO$_4$ nanoporous film. Four elements (including O, Bi, V, and Co) are distributed

uniformly over the whole sample (Fig. 4b, c, d, and e), suggesting the successful loading of CoO$_x$ cocatalysts. Quantitative EDS analysis reveals that the atomic Co/Bi ratio is 1.46:23.61, corresponding to an overall CoO$_x$ loading of ~5.8% (relative to BiVO$_4$). Although EDS is not a precise technique for determining the film composition, it confirms the existence of CoO$_x$ cocatalyst on the BiVO$_4$ surface.

Optical Absorption Properties

Figure 5a compares the UV–Vis absorption spectra and their corresponding Tauc plots for the abovementioned CoO$_x$/BiVO$_4$ electrode samples. Apparently, BiVO$_4$ displays an excellent visible-light response with a sharp absorption edge around 470 nm due to its wide bandgap of ~ 2.45 eV. Both the UV and visible-light absorption of BiVO$_4$ were enhanced significantly after surface modification with the CoO$_x$ cocatalysts due to the narrower bandgap of CoO$_x$ ($E_g = $ ~1.6 eV). With increasing the deposition time, the optical absorbance is enhanced over the entire band, indicating the effect of CoO$_x$ as a narrow-bandgap material. The 40-CB sample has the highest visible light absorption. Figure 5b shows the Tauc plot of nanoporous BiVO$_4$ and CoO$_x$/BiVO$_4$ films, which displays a bandgap of 2.45 eV for pure BiVO$_4$ through a linear fitting of the curve.

PEC Performance

Figure 6 compares the PEC performance of BiVO$_4$ nanoporous photoanodes before and after modifying with CoO$_x$ cocatalysts. It is found that the pristine BiVO$_4$ photoanode exhibits a photocurrent of 1.24 mA/cm^2 at 1.23 V_{RHE} under simulated solar irradiation. After modifying with CoO$_x$, the photocurrent density of BiVO$_4$ is enhanced significantly along with a reduction in the onset potential. The highest photocurrent density (3.36 mA/cm^2) at 1.23 V_{RHE} appears in the 20-CB sample, which is nearly three times that of the pure BiVO$_4$ photoanode. Apparently, the value is comparable with those reported in other published articles, as listed in Table I. The enhanced PEC performance might be ascribed to a more efficient visible light harvesting and a lowering of the interfacial charge transfer resistance. It is speculated that these CoO$_x$ cocatalysts act as the hole-extraction layer, leading to a significant enhancement of hole-injection efficiency (from photoanode to electrolyte). Nevertheless, it is strange that as the deposition time is further prolonged to 30 s or 40 s, the photocurrent (1.23 V_{RHE}) of the obtained sample decreases. Namely, 30-CB exhibits lower photocurrent than 20-CB, while that of 40-CB is even lower than that of 30-CB. Overall, 20-CB exhibits the highest PEC activity among all samples. Although the photocurrent of 40-CB is comparable to that of the unmodified BiVO$_4$ (1.23 V_{RHE}), the former has a significantly lower
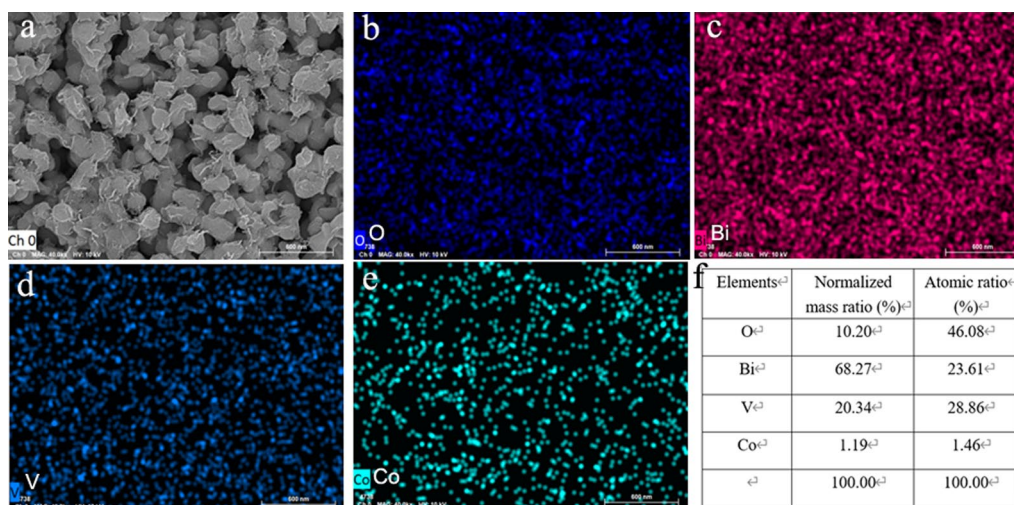
Fig. 4 Typical SEM image (a) and EDS elemental mapping data of a typical BiVO$_4$/ CoO$_x$ sample (40-CB) for the elements O (b), Bi (c), V (d), and Co (e). and total spectrum (f) in the 40-CB sample.
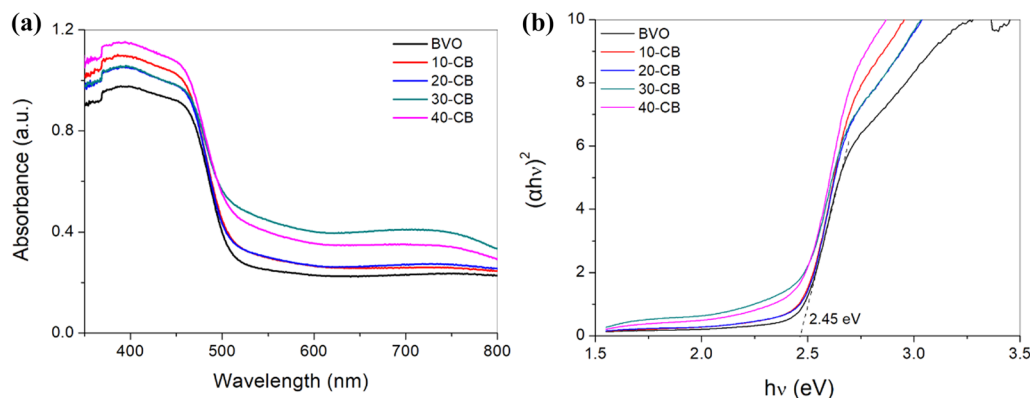

Fig. 5 (a) UV–Vis diffusion absorption spectra and (b) Tauc plots of BVO/CoO$_x$ samples with different CoO$_x$ deposition times (10–40 s).

onset potential than the latter. In addition, the applied bias photon-to-current conversion efficiency (ABPE) plots of the pristine BiVO$_4$ and BiVO$_4$/CoO$_x$ photoanodes are presented in Fig. 6b. The ABPE values were calculated using the following equation[19]:

$$\eta(\%) = \frac{J \times (1.23 - V_{RHE})}{P_{in}} \qquad (1)$$

where J refers to the photocurrent density (mA/cm), V_{RHE} refers to the applied bias, and P_{in} is the input light power intensity (100 mW/cm^2). As shown in Fig. 6b, 20-CB displays the maximum ABPE value of 0.72% at ~0.8 V_{RHE}, which is about four times that of pristine BiVO$_4$ (only 0.14% at 1.0 V_{RHE}). It is also noted that 20-CB exhibits the highest ABPE peak value of all, which is consistent with the aforementioned linear sweep voltammetry (LSV) results.

Figure 6c presents a comparison of the Nyquist plots of pristine BiVO$_4$ and BiVO$_4$/CoO$_x$ photoanodes under simulated solar irradiation, and the fitted results are shown in Table II. The Nyquist plots of all the samples consist of an arc and a semicircle, where the smaller arc shows the kinetics of charge transfer in the photoelectrode, while the larger semicircle represents the charge transfer resistance (R_{CT}) from the impedance at the solid/liquid interface. It was found that BiVO$_4$ had the largest semicircle diameter, indicating a high charge transfer resistance occurring at the solid/liquid interface. The CoO$_x$ loading can effectively reduce the interfacial transfer resistance, leading to the enhancement of the charge injection efficiency (towards the electrolyte). As a result, 20-CB has the smallest semicircle diameter and interface charge transfer resistance (39.0 Ω). However, a further increase in the deposition time would lead to a significant increase in the semicircle diameter (or R_{CT}). The
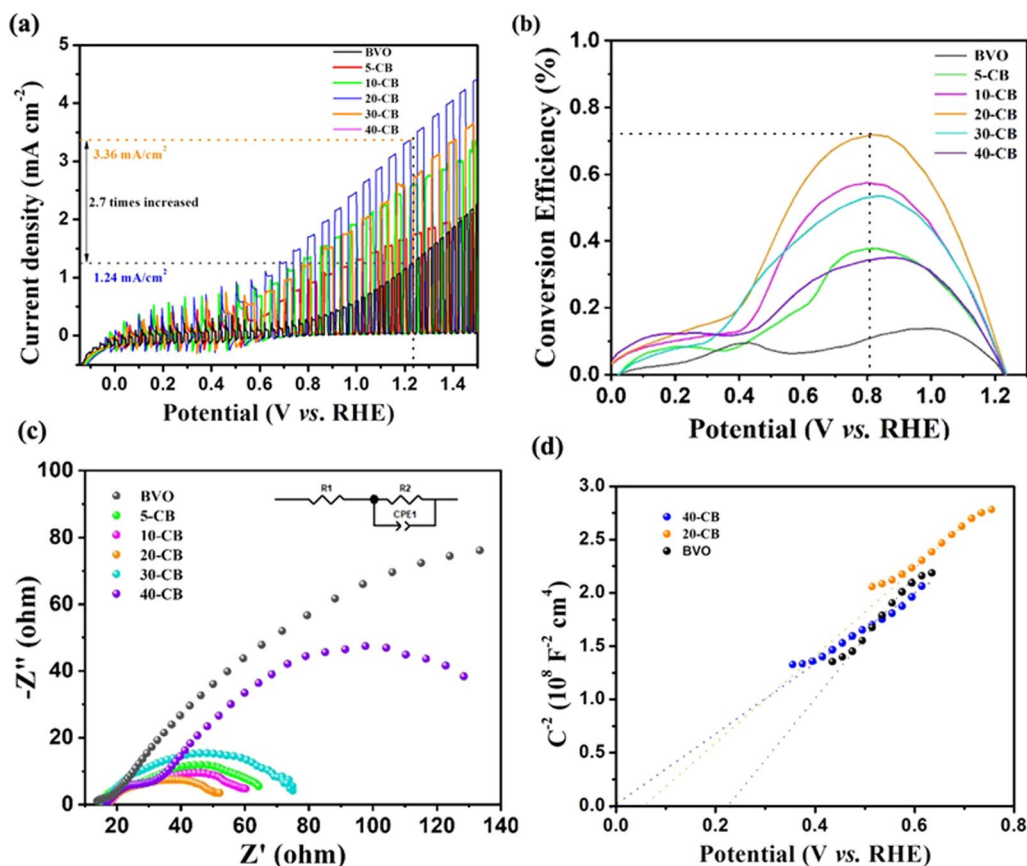
Fig. 6 (a) LSV plots, (b) APBE plots, (c) Nyquist plots, and (d) M–S plots of different photoanode samples under simulated solar irradiation. Note that the M–S plots are based on measurements in the dark. The inset in (c) displays an equivalent circuit model for fitting the Nyquist plots.

	Photoanode	Electrolyte	Photocurrent density at 1.23 V_{RHE}	Ref. (year)
Table I Comparison of the optimal PEC performance of BiVO$_4$-based photoanodes in the published articles with our present results. All measurements were carried out under simulated solar irradiation (AM1.5G)	CoO$_x$/BiVO$_4$	0.1 M Na$_2$SO$_4$ (pH = 7.0)	3.36 mA/cm^2	This work (2024)
	FeOOH/Au/BiVO$_4$	0.1 M Na$_2$SO$_4$ (pH = 7.0)	4.64 mA/cm^2	16 (2021)
	FeOOH/NiOOH/CoO$_x$/BiVO$_4$	0.5 M KPi (pH = 7.0)	6.34 mA/cm^2	10 (2021)
	MoOx/MXene/BiVO$_4$	0.5 M KBi (pH = 9.3)	5.58 mA/cm^2	11 (2022)
	CeQD/BiVO$_4$	0.5 M KPi (pH = 7.4)	4.0 mA/cm^2	12 (2022)
	CoFeBi/BiVO$_4$	0.5 M K$_3$BO$_3$ (pH = 9.3)	4.4 mA/cm^2	17 (2023)
	NiFeO$_x$/CuSCN/ BiVO$_4$	0.5 M KBi (pH = 9.3)	5.6 mA/cm^2	18 (2024)

In this table, KPi represents a KH$_2$PO$_4$ and K$_2$HPO$_4$ buffer solution, while KBi represents potassium borate (K$_3$BO$_3$).

Table II Calculated electronic parameters from the Nyquist curves under illumination

Sample	R_S (Ω)	R_{CT} (Ω)
BiVO$_4$	16.95	315.3
5-CB	13.44	65.2
10-CB	15.66	62.8
20-CB	16.37	39.0
30-CB	21.35	44.6
40-CB	16.42	151.9

40-CB sample displays a significantly higher R_{CT} value than the other BiVO$_4$/CoO$_x$ samples. This may be related to the thick coating layer, which increases the interfacial carrier recombination loss. This is also why an ultrathin cocatalyst layer is used in most reports. In other words, a larger number of holes are lost during the transport process before reaching the electrolyte. Figure 6d compares the Mott–Schottky (M–S) plots of BiVO$_4$, 20-CB, and 40-CB measured in the
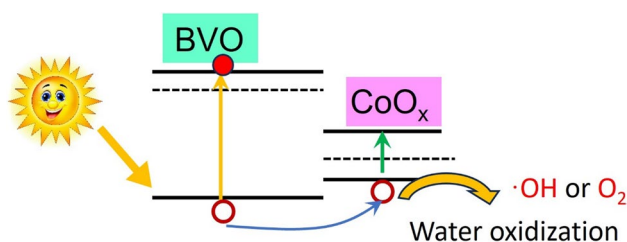
Fig. 7 Schematic model for the charge transfer process occurring at the BVO_4/CoO_x interface under solar illumination.

dark. It is known that both the carrier density (N_D) and flat-band potential (V_{FB}) of a semiconductor can be calculated from the M–S plots, since there is a direct relationship between N_D and V_{FB} as follows[20]:

$$\frac{1}{C^2} = \frac{2}{e\varepsilon\varepsilon_0 N_D}\left(V - V_{FB} - \frac{kT}{e}\right) \qquad (2)$$

$$N_D = \frac{2}{e\varepsilon\varepsilon_0}\left[d\left(\frac{1}{C^2}\right)/dV\right]^{-1} \qquad (3)$$

where C is the depletion layer capacitance, $e = 1.6 \times 10^{-19}$ C, ε is the dielectric constant (68 for $BiVO_4$), ε_0 is the permittivity in vacuum (8.85×10^{-12} F/m), A represents the active irradiation area, V is the applied potential, and kT/e is a temperature-dependent correction term. As shown in Fig. 6d, the $BiVO_4$ photoanode displays an N_D value of 3.76×10^{19} cm^{-3} with a V_{FB} value of 0.22 V. The modification of CoO_x cocatalyst reduces V_{FB} of $BiVO_4$ significantly while increasing the carrier concentration. The 20-CB sample shows a low V_{FB} value (0.05 V_{RHE}), while 40-CB shows a lower V_{FB} value (just 0 V_{RHE}). That is to say, the V_{FB} decreases with increasing the CoO_x deposition time, of which the variation trend is consistent with that of the onset potential (Fig. 6a). Obviously, the negative shift of V_{FB} is beneficial for achieving better PEC performance, which depends not only on V_{FB}, but also on several factors including visible-light absorption and interfacial transfer resistance.

Figure 7 presents a schematic model to reveal the mechanism for the enhanced PEC activity of a $BiVO_4$ photoanode. As can be seen, CoO_x acts as an oxygen evolution reaction (OER) cocatalyst. Under solar illumination, the electrons inside $BiVO_4$ are excited, leaving the holes in the valence band (VB). Due to the loading of CoO_x cocatalysts, the holes migrate to the VB of CoO_x for water oxidation (into ·OH or O_2). Apparently, the CoO_x loading not only increases the carrier concentration in photoanode, but also enhances the band bending at the solid/liquid interface, leading to a more negative V_{FB}. Although the V_{FB} value becomes more negative, 40-CB still shows much lower PEC activity than 20-CB, which may be associated with its larger interfacial

transfer resistance, as mentioned before (Fig. 6c). It is well known that increasing the deposition time is beneficial for achieving a thicker CoO_x layer, leading to an increase in the interfacial transfer resistance value.

Conclusion

In summary, $BiVO_4$ nanoporous photoanodes were modified with CoO_x cocatalysts through a facile electrodeposition route. The successful loading of CoO_x cocatalysts was verified by EDS mapping, XRD, and PEC measurements. It was found that the PEC activity of $BiVO_4$ was greatly influenced by the electrodeposition time. Loading CoO_x can enhance visible-light absorption and reduce the onset potential, resulting in higher photocurrent (1.23 V_{RHE}). Nevertheless, extending the electrodeposition would result in a significant reduction of the PEC activity. The optimal PEC activity was obtained with the 20-CB sample (with a deposition time of 20 s). Although 40-CB has a similar photocurrent at 1.23 V_{RHE} with the $BiVO_4$ sample, the onset potential of the former is much lower than the latter. We hope that this study will contribute to a deeper understanding of the semiconductor PEC process.

References

1. T. Hisatomi, J. Kubota, and K. Domen, *Chem. Soc. Rev.* 43, 7520 (2014).
2. R. Tang, S. Zhou, Z. Zhang, R. Zheng, and J. Huang, *Adv. Mater.* 33, 2005389 (2021).
3. J.H. Kim, D. Hansora, P. Sharma, J.W. Jang, and J.S. Lee, *Chem. Soc. Rev.* 48, 1908 (2019).
4. T. Li, J. He, B. Peña, and C.P. Berlinguette, *Angew. Chem. Int. Ed.* 55, 1769 (2016).
5. Q. Wang, J. He, Y. Shi, S. Zhang, T. Niu, H. She, Y. Bi, and Z. Lei, *Appl. Catal. B Environ.* 214, 158 (2017).
6. X. Li, J.Q. Wan, Y.W. Ma, Y. Wang, and X.T. Li, *Chem. Eng. J.* 404, 127054 (2021).
7. B. Zhang, H.P. Zhang, Z.Y. Wang, X.Y. Zhang, X.Y. Qin, Y. Dai, Y.Y. Liu, P. Wang, Y.J. Li, and B.B. Huang, *Appl. Catal. B Environ.* 211, 258 (2017).
8. P.M. Rao, L. Cai, C. Liu, I.S. Cho, C.H. Lee, J.M. Weisse, P. Yang, and X. Zheng, *Nano Lett.* 14, 1099 (2014).
9. C. Zachaus, F.F. Abdi, L.M. Peter, and R. van de Krol, *Chem. Sci.* 8, 3712 (2017).
10. B. He, S.R. Jia, M.Y. Zhao, Y. Wang, T. Chen, S.Q. Zhao, Z. Li, Z.Q. Lin, Y.L. Zhao, and X.Q. Liu, *Adv. Mater.* 33, 2004406 (2021).

11. Y.R. Song, X.M. Zhang, Y.X. Zhang, P.L. Zhai, Z.W. Li, D.F. Jin, J.Q. Cao, C. Wang, B. Zhang, J.F. Gao, L.C. Sun, and J.G. Hou, *Angew. Chem. Int. Ed.* 61, e202200946 (2022).

12. D.H. Seo, S.Y. Hong, T.H. You, A. Sivanantham, and I.S. Cho, *Chem. Eng. J.* 450, 137917 (2022).

13. Z.Y. Liu, X.F. Wu, B.N. Zheng, Y. Sun, C.M. Hou, J. Wu, K.K. Huang, and S.H. Feng, *Chem. Commun.* 58, 9890 (2022).

14. T.T. Pan, Y.M. Tang, Y.X. Liao, J.C. Chen, Y.P. Li, J. Wang, L.S. Li, and X. Li, *Mol. Catal.* 549, 113527 (2023).

15. R. Yalavarthi, R. Zbořil, P. Schmuki, A. Naldoni, and Š Kment, *J. Power. Sources* 483, 229080 (2021).

16. H.M. Geng, P.Z. Ying, Y.L. Zhao, and X.Q. Gu, *Int. J. Hydrog. Energy* 46, 35380 (2021).

17. X.J. Zhao, Y.F. Rui, Y. Bai, J.W. Huang, H.D. She, J.H. Peng, and Q.Z. Wang, *CrystEngComm* 25, 6677 (2023).

18. J.K. Wang, J.D. Sun, Y.L. Liu, X. Zhang, K. Cheng, Y.P. Chen, F.Z. Zhou, J.J. Luo, T.B. Li, J.J. Guo, and B.S. Xu, *J. Colloid Interface Sci.* 666, 57 (2024).

19. Z. Li, W. Luo, M. Zhang, J. Feng, and Z. Zou, *Energy Environ. Sci.* 6, 347 (2013).

20. H.P. Maruska and A.K. Ghosh, *Sol. Energy* 20, 443 (1978).